ENGINEERING

Polymorphic display and texture integrated systems controlled by capillarity

Jonghyun Ha^{1,2}†, Yun Seong Kim^{1,3}†, Chengzhang Li¹, Jonghyun Hwang¹, Sze Chai Leung¹, Ryan Siu¹, Sameh Tawfick^{1,3}*

Soft robotics offer unusual bioinspired solutions to challenging engineering problems. Colorful display and morphing appendages are vital signaling modalities used by natural creatures to camouflage, attract mates, or deter predators. Engineering these display capabilities using traditional light emitting devices is energy expensive and bulky and requires rigid substrates. Here, we use capillary-controlled robotic flapping fins to create switchable visual contrast and produce state-persistent, multipixel displays that are 1000- and 10-fold more energy efficient than light emitting devices and electronic paper, respectively. We reveal the bimorphic ability of these fins, whereby they switch between straight or bent stable equilibria. By controlling the droplets temperature across the fins, the multifunctional cells simultaneously exhibit infrared signals decoupled from the optical signals for multispectral display. The ultralow power, scalability, and mechanical compliance make them suitable for curvilinear and soft machines.



NonCommercial

License 4.0 (CC BY-NC).

INTRODUCTION

Natural creatures have fascinating morphing skin appendages with switchable functionalities. Chameleons camouflage by exploiting their pixelated skin appendage (see Fig. 1A) (1). Animals use liquid media to control these pixelated appendages. Beautiful skin patterns are created on demand either by stretching ink-filled elastic sacs (chromatophores in cephalopods) (2) or by secreting/draining liquids from porous photonic structures (tortoise beetle) (3). Moreover, fluids are used to morph skin appendages, for instance, by bundling thin hairs in the otters fur or the beetles feet for temperature regulation or switchable adhesion, respectively (4-5). The critical advantages to these skin display and texture morphing mechanisms are their multimodality (color, temperature, texture, and adhesion), multifunctionality (camouflage and temperature regulation), and mechanical flexibility, while using only ultralow power compared to energy-intense light-emitting semiconductor devices. In nature, dynamically changing appendages have state persistence, i.e., the ability to use low power to switch the display, and then retain the new state with minimal energy cost. While some of these individual functions have been explored recently using fluid networks (6) or inflatable skins (7–8), these demonstrations remain limited by preprogrammability, single modality, switching speed, and the high-power requirement for state switching and retainment.

Here, we studied flexible appendages, which flap to large angles by the hydrodynamic action of liquid droplets, drawing inspiration from the capillary bundling of the hair of otters and beetles. The ultrasoft fins are fixed at the base to wet cells, named flap-phores and spelled here "flap4." The wet cells are intended to operate in arrays forming pixelated skins, where each cell is individually switched by liquid control via an epidermal pore. The pore is

connected to a fluid network, valves, and motorized syringes, but many other sources of liquid pressure can work for these small volumes (9-10). The flapping fin switch between two intriguing stable drained states: straight and bent, which are normal and parallel to the substrate, respectively. The switching is controlled by the rate of drainage from the epidermal hole located next to the fin on one side. At slow drainage, the fins exhibit a capillarity-dominated operation mode where the fin flaps to the narrow side (N mode), and at high drain rate, we observe a suction pressure-dominated mode where the fin flaps to the wide side (W mode). We derive simple scaling law to capture the intriguing physical phenomenon responsible for switching between the N mode and the W mode, which belongs to the broad class of elastocapillarity (11-12), and specifically dynamic elastocapillarity where hydrodynamics plays a dominant role (13-15). In the rest of this report, we show more complex dynamic elastocapillary polymorphism useful for a variety of multimodal signaling devices. We exploit the flap4 cells in constructing soft multipixel display—where each flap4 cell is an individually controlled pixel—and in optical/infrared (IR) multispectral signaling by leveraging the contrast between the fin color and the cells background and by using droplets of different temperatures across the fin to create IR contrast simultaneously. By this demonstration, it is shown that these new capillary flapping phenomena and the multimodal signaling and texture morphing can be added to the repertoire of future reflective display devices, particularly suitable for soft and conformable needs.

RESULTS

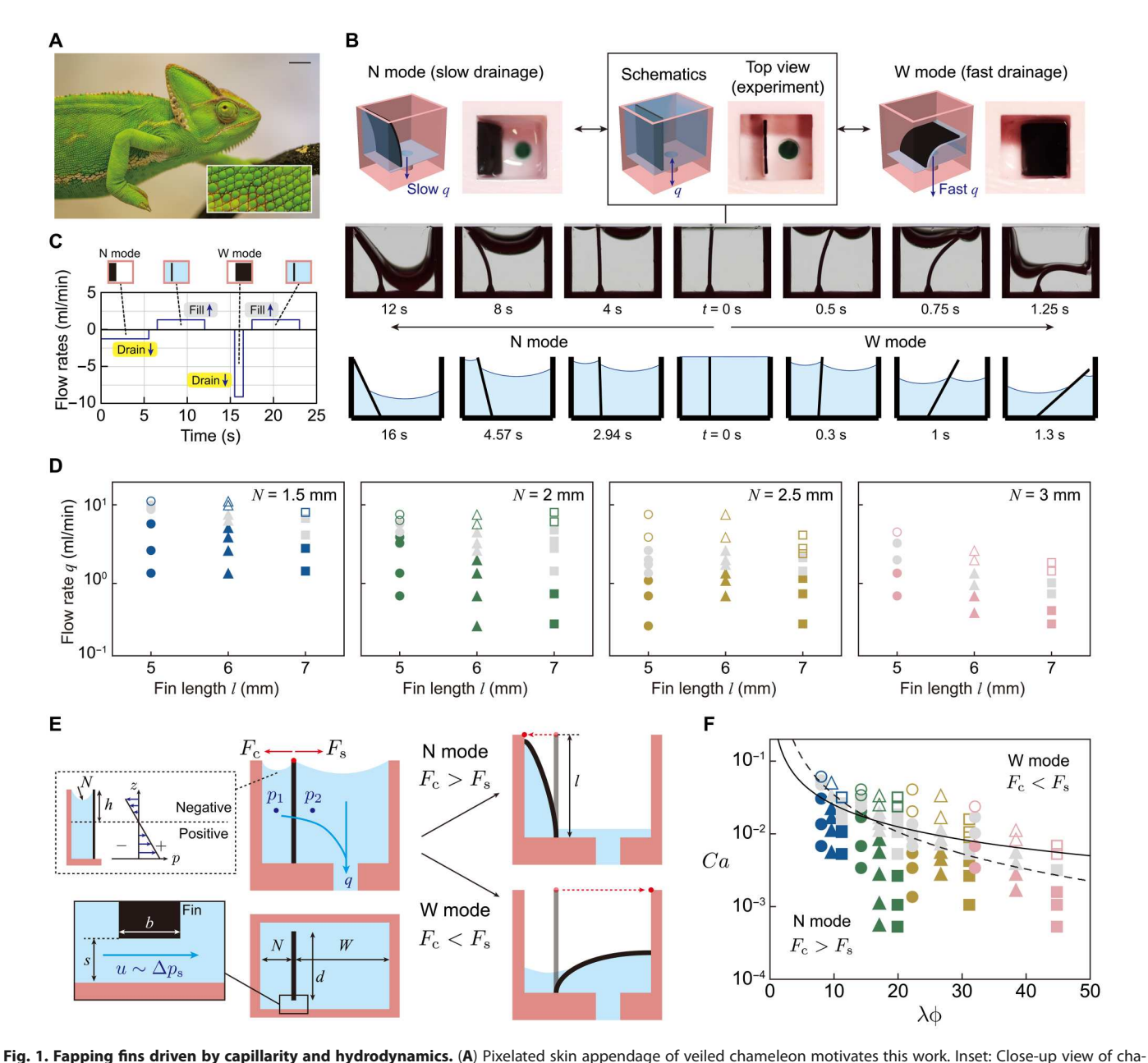
Basic concept of bimorphic fin

A bimorphic flap4 is shown in Fig. 1, and a video of its operation is shown in movie S1. When the chamber is filled with liquid, the fin is vertical because of liquid pinning at the upper corner of the fin. As the liquid is slowly drained through the pore, which is on the wide side (W mode) of the cell, the fin is attracted to the wall on the narrow side (N mode). This behavior is intriguing as it appears that the negative pressure of the liquid drainage is pushing the fin

¹Department of Mechanical Science and Engineering, University of Illinois at Urbana-Champaign, Urbana, IL 61801, USA. ²Department of Mechanical Engineering, Ajou University, Suwon 16499, Republic of Korea. ³The Beckman Institute for Advanced Science and Technology, University of Illinois at Urbana-Champaign, Urbana, IL 61801, USA.

^{*}Corresponding author. Email: tawfick@illinois.edu

[†]These authors contributed equally to this work.



reg. 1. Papping this driven by capitality and hydrodynamics. (A) Pixelated skin appendage of Vehed Charlested Historical Regions and Pixelated skin appendage of Vehed Charlested Historical Regions (A) Pixelated skin appendage of Vehed Charlested Historical Regions (B) Bimorophic fin. The middle images show the snapshots for both modes in the side view, where N mode (q = 1.3 ml/min) starts from center to right (see movie S1). The fin length is 5 mm, and the working fluid is mineral oil. The bottom images are snapshots from the numerical simulation (see movie S2). (C) Plot of the drain flow control signal versus time. Positive and negative signs of the y axis correspond to supply and drainage of liquid, respectively. (D) Experimental fin flapping regime map with the fixed W = 4 mm. Circle, triangle, and square symbols correspond to I = 5, 6, and 7 mm, respectively. Blue, green, brown, and light pink colors correspond to N = 1.5, 2, 2.5, and 3 mm, respectively. The total width $N + W \times 5.5$ 5.5, 6, 6.5, and 7 mm, with negligible fin thickness. The gray color corresponds to the transition between N mode and W mode. (E) Mechanism of fin deformation modes. Drainage to the epidermal hole drives two flow paths: along the fin and the across s. The dashed inset corresponds to the profile of the pressure gradient along the fin length. The solid inset illustrates leak velocity driven by the suction pressure within s. (F) Universal regime map based on a theoretical model. Top and bottom regimes from the theoretical line correspond to W mode and N mode, respectively. In the theoretical line, we use the prefactor = 0.25 to precisely fit the experimental results. The dashed line corresponds to the numerical model (see section S5). All symbols are described in the caption (D).

away to the other side of the wet cell. By increasing the flow rates enforced by the syringe pump, q, we observe that the fin transitions from bending toward the narrow side, N mode, to flapping toward the wide side where the negative suction pressure is applied, the W mode. Example of this behavior is shown in the top and side view in Fig. 1B. Figure 1C shows the systematic plot of flow rates to obtain two modes of flap4. To enable this behavior, the fins must be extremely soft; otherwise, their bending stiffness restricts the large deformation associated with the W mode. The extreme compliance enables the fins to persist in the drained state whether it is N mode or W mode (see section S1). This persistence in both states is due to the capillary forces being one order of magnitude higher than the elastic restoring force in either of the straight (N mode) or bent (W mode) configurations. This compliance is achieved using a soft polymer polyvinylsiloxane (Zhermack Elite Double 8) by molding in a precisely fabricated negative mold (see Supplementary Materials and Methods). The fin thickness, b, is typically less than 0.5 mm, and its width, d, is in the range of 5 mm. The fin recovers its original position when the cell is refilled with the liquid. We experimentally determined the threshold flow rate q above, which the fin switches to the W mode flapping. We observe that the threshold q for the W mode flapping decreases with the increase in fin length, *l*, or the narrow side width, N, as shown in Fig. 1D. We additionally perform an experimental parametric analysis to investigate the association between the width of the narrow side N and the wide side W (see section S2). The symbol s represents the distance between the fin and the wall in the direction of the fin width, as illustrated in Fig. 1E. In the experiment, we keep W = 4 mm and the gap s = 0.4mm. The working liquid is mineral oil.

To understand the mechanism of bimorphic fin bending to the narrowN side and flapping to the wideW side, we consider the fluid flow path when the liquid is drained through the pore (Fig. 1E) located at the bottom surface of the wide side. While the drainage within the wide side is dominated by the downward flow toward the pore, the drainage from the narrow side, N, is driven by flow leaking through the small spacing s where the liquid experiences a large viscous pressure drop. It is this restriction of the leakage flow that pulls the fin to the wide side due to the high suction pressure created $\Delta p_{\rm s} = p_1 - p_2$. We note that suction pressure increases with the leakage velocity, u, so the fin flaps to the W mode only at drain rates higher than a certain transition threshold (i.e., fast u). When the drain rate is slower than this transition threshold, the meniscus between the fin and the wall in the narrow side pulls the fin to the narrow side due to the Laplace pressure, $\Delta p_c \sim \gamma \kappa$, where γ is the surface tension and κ is the curvature of the meniscus of the liquid. Since the fin has negligible stiffness, it flaps toward the narrow mode at low drain rate due to the negative capillary pressure. As the drain rate is increased, the balance between Δp_s and Δp_c describes the transition between the two states N and W modes.

Scaling law of capillary-induced bimorphing

To theoretically predict the transition flow rate q shown in Fig. 1E, we balance the forces acting on the fin: capillary due to the curvature of the meniscus and suction due to the hydrodynamic drainage flow. In the simplest model, we assume that the liquid meniscus pulls the soft fin to the narrow side since N < W (strong capillary pressure at N) and ignore the capillary force pulling to the wide side. The capillary force acts in accordance with the negative pressure region above a certain height, so it is governed by the effective

area, $A_{\rm e}$ (see the dashed inset of Fig. 1E). We express the effective area by Jurin's height, $h \sim \gamma/(\rho g N)$, so $A_e = hd$; and ρ and g are liquid density and gravitational acceleration, respectively. Jurin's height is considered here because the fin is longer than the capillary rise. The dashed inset of Fig. 1E depicts the negative pressure region within *N*. Combining capillary pressure, $\Delta p_c \sim \gamma/N$ and the effective area, hd, we express the force, $F_c \sim \gamma hd/N$. This force dominates the bending of the fin toward the narrow side at quasi-static drainage. However, as the flow rate increases, a dynamic suction pressure, Δp_s , develops because of drainage and acts in the opposite direction to the capillary force. We theoretically estimate Δp_s regulated by the Poiseuille flow within the narrow gap, s, as described in the inset of Fig. 1E. The suction pressure driving the viscous liquid flow is $\Delta p_{\rm s} \sim \mu u b/s^2$. Obeying the flow continuity, u can be generally expressed as $u \sim q/(ls)$. Combining suction pressure $\Delta p_s \sim \mu ub/s^2$ and the fin surface area dl, we obtain the pulling force, $F_s \sim$ $\mu ubdl/s^2$. In the current experiments, $b \sim s$, so $F_s \sim \mu udl/s$. This force dominates the bending of the fin toward the wide side at high flow rate.

The competition between the capillary and suction forces, $F_c \sim F_s$ ($\gamma hd/N \sim \mu udl/s$), provides insight into the transition of behavior between W mode and N mode. When $F_c < F_s$ (W mode), the fin eventually flaps to the wide side because the suction exceeds the capillary bending at N. When $F_c > F_s$ (N mode), where the suction pulling is not enough to overcome the capillary forces, the fin bends to the narrow side. The force balance, $F_c \sim F_s$, gives

$$Ca \sim (\lambda \phi)^{-1}$$
 (1)

where $Ca = \mu u/\gamma$ is the capillary number, $\lambda = l/h$ is the dimensionless Jurin's height, and $\phi = N/s$ is the leakage ratio. We plot the universal regime map divided into two distinct modes using the scaling law, as shown in Fig. 1F. The scaling law of Eq. 1 includes various dimensionless numbers: the dynamic to capillary effect ratio (Ca), capillary effects (λ), and the leakage ratio (ϕ). In the high dimensionless number (Ca and $\lambda \phi$) regime (fast u, large N, and long l), the fin flaps to the W mode, while N mode is observed when Ca and $\lambda \phi$ are small. Further, we use different liquids to confirm that the scaling law quantitatively explains the viscous effects (see section S3). This theoretical analysis provides a priori prediction of texture-shifting materials driven by dynamic capillarity, which allows us to precisely design this unusual capillary-hydrodynamic flapping. Two distinct modes are observed when the fins are extremely soft and within a range of the conduit geometries (N, W, and s), as predicted by the simple scaling model. When the stiffness of the fin is higher than a certain the threshold, the fins always pierce the liquid interface, and the two modes are suppressed (see section S4). The scaling law, while insightful, greatly simplifies the complex physics of flap4s. For instance, the Bond number (ratio of gravitational to capillarity) is on the order of 1, and hence, the hydrostatic pressure plays some role in the device operation. In addition, the intricate balance of capillary forces from the two menisci on both sides plays a role in the threshold q for the transition. Accordingly, we have also constructed a two-dimensional (2D) reduced order elastocapillary hydrodynamic model (see section S5). This reduced-order model has the main elements of the device: capillary forces from both chambers, gravitational forces, and hydrodynamic lubrication between the soft fin and the walls acting on a rotating fin connected to the substrate by a torsion spring. This more elaborate model shows the

existence of a threshold flow rate for each device at which the fins move to the wide side. Video simulations of the flap4s are in the Supplementary Materials, and snapshots are extracted in the bottom images of Fig. 1B. The transition threshold predicted by the reduced order model also captures the experimental results but does not fully agree with the scaling law (see the dashed line in Fig. 1F), which is expected because the scaling law is extremely simplified, not considering the fin elasticity (the extreme compliance limit), capillarity on both sides or the gravitational forces.

Multimodal texture morphing appendage

Beyond the bimorphing flapping fin, more complex, polymorphic flap4s are constructed with multiple fins and drain pores having multiple flapping modes. For instance, the double-fin cell shown in Fig. 2A shows four modes: blooming, flopping to the right, flopping to the left, and piercing. At slow drainage from any side or both sides simultaneously, the two fins coalesce and pierce the liquid interface, reminiscent of the N mode but for a symmetric cell. Fast drainage from both sides causes the fins to both bend outward, and this blooming mode is reminiscent of the W mode. Fast drainage from only one side causes both fins to flop toward that side following the flow. Considering the double fin to be the symmetric construction of two mirrored single fins, the theoretical model of the single fin (Eq. 1) is used to capture the two distinct regimes of the double fins (piercing and flopping), as shown in Fig. 2B.

With four flapping fins and two drain holes at the extremities, we obtain five-mode polymorphic flap4 cells, as shown in Fig. 2C. In particular, the flapping of four fins is reminiscent of flopping dominos, and their texture relies on the speed and direction of drainage. The symmetric cases of all flapping to the right or to the left are achieved by high drain rate from one direction, while the symmetric blooming mode is achieved by high drain rate from both pores simultaneously. On the other hand, the symmetry breaking configurations are obtained by controlling the timing of drain onset. For instance, when we first drain from the left side and then drain from the right side after a few seconds, only the leftmost three fins flap to the left, while the right most fin flaps to the right sides. This creates the symmetry breaking modes. Last, in Fig. 2D, we present radial and 3D flap4s such as blooming flowers where each fin behaves as a petal. These exhibit blooming (side drainage) and closing (hole drainage) modes, as shown in Fig. 2D. We provide the systematic flow data in each texture geometry, as shown in the plots located at the bottom of Fig. 2 (A, C, and D). As can be seen from these polymorphic examples, the interplay between onset of drainage and drain rates can be freely programmed and reprogrammed to produce far more complicated morphable texture material systems.

Multipixel soft display devices

By combining an array of flap4 cells, we construct a multipixel multimodal soft display panel. Each pixel has a flapping fin that reflectively produces an on/off black contrast because of the dark blue color of the fin, which creates a contrast against the yellow color of the background. Figure 3A illustrates the mechanism of a single fin flapping motion controlled by pore drainage. Unlike the previous experimental setup, we here design a shorter wall than the fin length and use water for the working fluid. Since the wettability between water and silicone is not favorable, the curvature of the liquid meniscus is convex (see Fig. 3A). By using this configuration,

we can show a single mode (only on/off mode) regardless of the drain rates. This flapping exhibit reversible on/off behavior, so that individual pixels can be dynamically and independently addressed. We construct a multipixel array (three by three) each controlled by selective channel drainage, as shown in Fig. 3B. The fabrication method is illustrated in Fig. 3C. When we drain the liquid from an open pore, the fin flaps to the horizontal configuration and remains there due to the trapped meniscus, thus persisting in the ON state. By individually addressing the pixels, the soft display forms characters (e.g., UIUC), as shown in Fig. 3D. We note that recent innovations in microscale pneumatic and hydraulic network can be adopted to produce high-resolution displays with low energy (10). Last, we compare with the conventional displays to provide a competitivity of the concept display composed of flap4 cells (see section S6).

IR camouflage of binary signal systems

Last, because we use liquid droplets to activate the flap4 cells, we exploited the effect of liquid temperature on creating IR patterns in addition to the optical reflective patterns. This is motivated by innovations in IR and multispectral imaging modalities in some animals—refer to recent advances in hyperspectral imaging (16-17). We designed the system to independently control the IR pattern by connecting liquid sources of various temperatures to specific pores on each cell. Our design also ensures that the fins can flap into two stable configurations, right or left, while creating a sharp temperature gradient across these two sides using the liquid flow through the pore. This results in a simultaneous multisignal optical/IR encoding systems. For one of the working examples (see Fig. 4A), we first fill the cold liquid in the chamber and then drain it on the right side. This results in the fin flopping to the right side. After flopping, we supply the hot liquid on the left side to distinguish the temperature signal in the IR domain. By the combination of liquid temperature and drainage location, we can develop three-digit binary encoding materials, showing a total of eight distinct device states. Code description is explained in Fig. 4B. The first left digit indicates flopping direction (L or R), which corresponds to the optical domain, and the middle and last digits correspond to the liquid temperature of the left and right side (H or C), which corresponds to the IR domain. The table of the IR/ optical signals is shown in the bottom images of Fig. 4B.

To demonstrate a full sequence of optical/IR encoding, we set the liquid (mineral oil) temperature at 22°C for cold and 50°C for hot and then sequentially fill and drain the liquid by various combinations to sequentially obtain the eight device states (movie S7). The full sequence is recorded, and the plots describing the flow control sequence and the corresponding screenshots are shown in Fig. 4C. Every first drainage leads to the fin flopping. For different temperature situations (CH or HC), we redrain the supplied liquid after flopping to avoid mixing issues and conserve the initial empty state, corresponding to reset shown in flow plots. This novel encoding system can produce two different signals in two different domains, so it can also be used in IR or optical camouflage devices. As an example, we show two scenarios of multisignal encoding: graphical and binary (see Fig. 4D). In the graphical example, the contrast form by the pixels draws an overall shape on the multipixel display such as the OK. Simultaneously, the temperature gradients across each pixel graphically draw another signal, here shown as NO. In addition to this scenario, we envision other scenarios

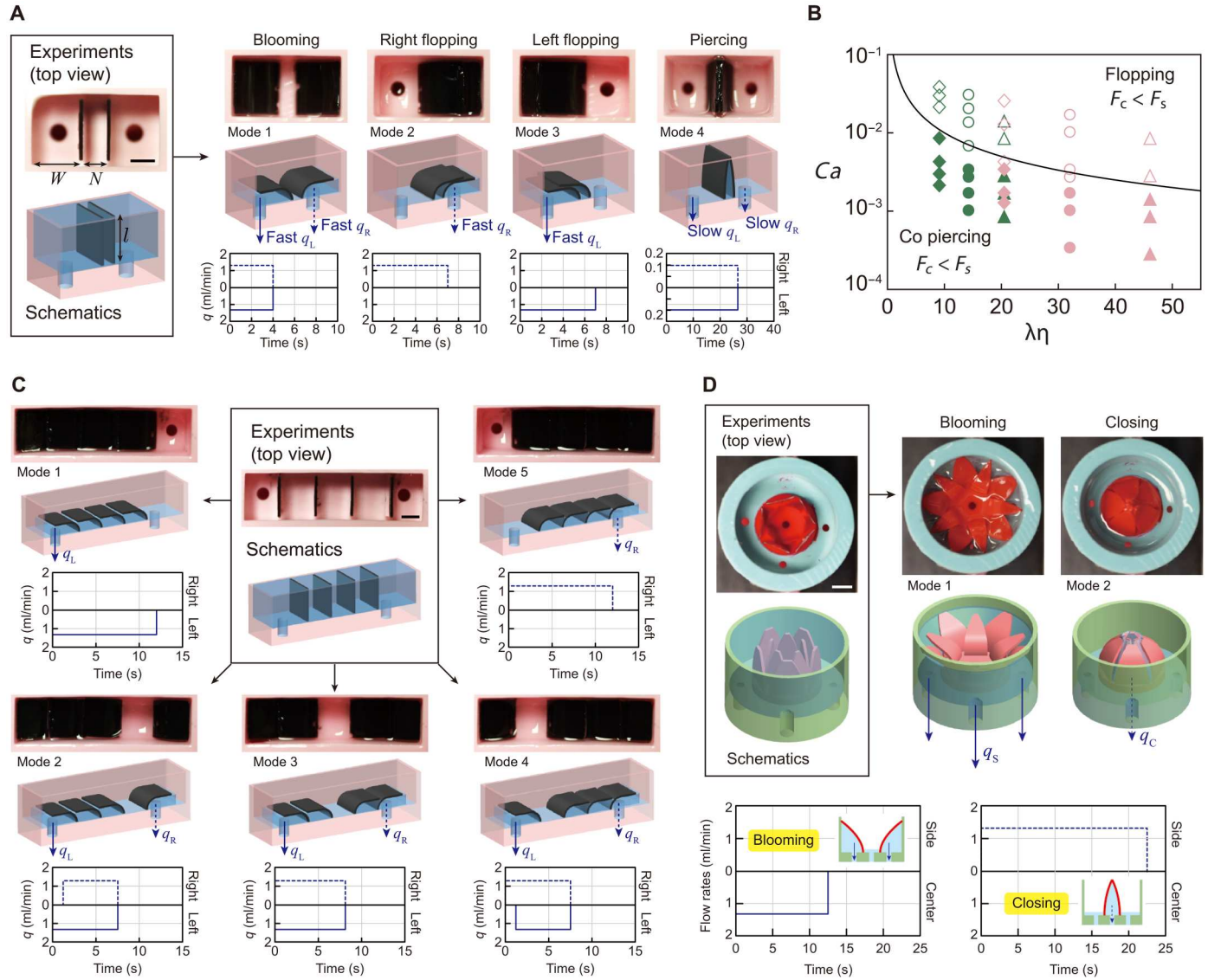


Fig. 2. Polymorphic and blooming fins. (A) Two fins perform four modes (piercing, right flopping, left flopping, and blooming), depending on the drainage location and speed (see movie S3). Top and bird views are the experimental images and 3D schematics, respectively. For piercing mode, q = 0.13 ml/min. For flopping and blooming modes, q = 1.3 ml/min. q_R and q_L correspond to the right and left drain rates, respectively. (**B**) Universal regime map for double fins. In the theoretical line, we use the prefactor = 0.1. Diamond, circle, and triangle symbols correspond to l = 4, 5, and 6 mm, respectively. Green and light pink colors correspond to N = 2 and 3 mm, respectively. (**C**) Domino-like collapsing texture (see movie S4). Array structures (four fins) show five modes by controlling the timing of the liquid flow. We get a symmetric mode (the left and right two fins collapse to the left and right side, respectively) when draining at both starts at the same time. Flow rates, q = 1.3 ml/min. q_R and q_L correspond to the right and left drain rates, respectively. (**D**) Texture mimicking flower (see movie S5). Draining at the side and center holes results in flower blooming and closing, respectively. Flow rates, q = 1.3 ml/min. q_S and q_C correspond to drain rates at the side and center, respectively. The plots located at the bottom of the schematics (A, C, and D) correspond to the liquid flow data in each mode. The working fluid for all systems is mineral oil. Systematic plots of the flow control are placed at the bottom of each 3D schematics. Scale bars, 2 mm.

where the individually controlled pixels draw bits of a binary code, both for the optical and IR message, such the example where we use an array to simultaneously encode the word UIUC in the optical domain and ILLINOIS in the IR domain (see section S7).

DISCUSSION

In summary, we studied the intriguing flapping of ultrasoft fins under the action of capillary hydrodynamic liquid effect. We demonstrated a soft robotic texture morphing cells and imparted contrast switching in addition to the texture change using the contrast of a flapping fin against the background color. These cells are driven by liquid droplets fed to the cells via epidermal pores and connected to a fluidic network underneath the cells. We show that the fin-flapping motion is governed by the balance between capillary forces and dynamic suction forces from the fluid network and show that the negligeable stiffness of the fins enables the flapping and the persistence of the fin state without external

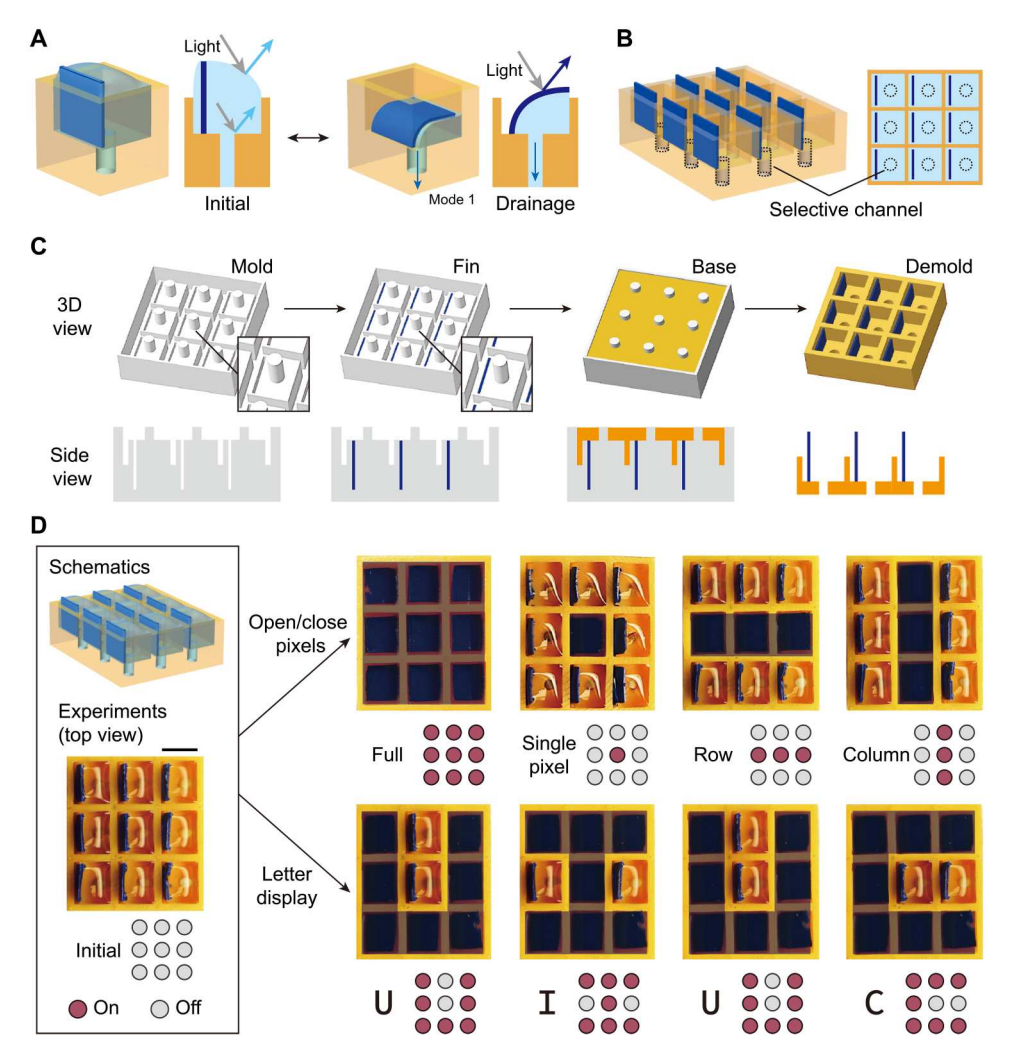


Fig. 3. Multipixel soft display devices. (A) Working mechanism of a single pixel. Depending on the liquid drainage, the fin bends toward the drainage hole. At an initial configuration, light (gray arrow) is reflected off the bottom of the device. At the bent configuration, light (gray arrow) is reflected off the fins (dark blue arrow). (B) Schematics of the selective channel (the dashed columns). Clogging and opening hole by selective channel provide on/off modes if the fin deforms or not. (C) The fabrication method of the soft cells is based on molding the full device and dying the fin. (D) The results of the soft display of the three-by-three panel (see movie S6 and fig. S7). The black box indicates the initial state. The red and gray colors correspond to open and closed holes, respectively. We show open/close pixels at the top row and letter display at the bottom row. The working fluid for the display is water and q = 0.5 ml/min. Scale bar, 4 mm.

power. Various polymorphic cells including two- and four-fin domino-like texture, blooming flowers, and multipixel can display patterns or alphanumerical letters. Droplets of contrasting cold and hot temperature are used for optical/IR multispectral message encoding, a concept that, to our knowledge, only exists in natural creatures. Since the driving force for the shape transition is surface tension, a wide variety of off-the-shelf materials work with this concept reliably, which we view as an advantage over highly specialized stimuli-responsive materials, which require complex synthesis and has a performance that degrade with time. The flap4 cells respond reasonably fast (a fraction of a second to a few seconds), which is considerably faster than diffusion-driven swelling polymers (hundreds of seconds). Since each cell requires only a few milliliters (\approx 0.2 ml) to operate, this concept can be integrated into large pixels by leveraging recent advances in microfluidic network components such as valves and pumps. This morphing texture can be leveraged in switchable multimodal antenna and transformable

electrical circuits. Overall, dynamic skin displays will add critical functionalities to soft machines (18–19), robots (20–21), and morphing fabrics (22). To accomplish this, we present a performance evaluation of flap4 on curved surfaces (see section S8).

Capillary-based morphing texture system can hold the potential to notably benefit the large-scale signage industry by offering substantial improvements in energy efficiency. This system can be used for extensive signage applications, such as those found in stadiums or on building rooftops. The possibility of larger soft display devices is demonstrated in Fig. 3, where a feasibility test was conducted to showcase a three-by-three multipixel configuration. While the current morphing system necessitates an external light source for displaying visible signs, it can still function as an effective reflective display during daylight hours. A primary advantage of the capillary-based robotic system is its energy efficiency, consuming approximately 10 W for a 100-m² screen size when the pixel size is approximately 1 mm. In contrast, light-emitting diode displays consume

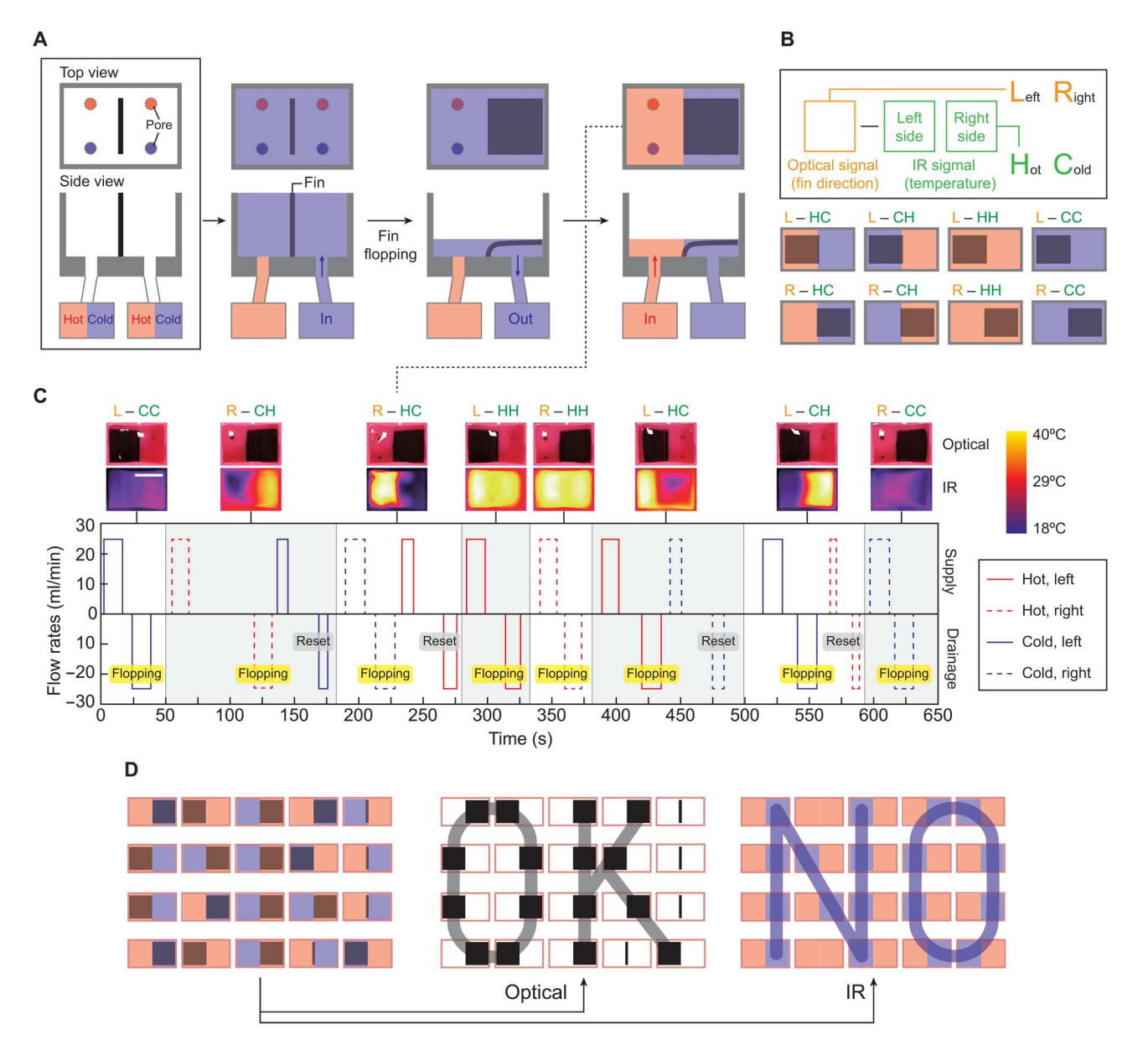


Fig. 4. Optical IR multispectral display. (**A**) Schematics of the working mechanism. To supply and drain the cold and hot drops, two holes connected to the syringe pumps are positioned at the left and right bottom surfaces. The detailed mechanism is written in the section IR camouflage of binary signal systems. (**B**) Three-digit encoding system. Combining three digits, we obtain a total of eight encoded states. The black box indicates the code description. The orange and green colors correspond to the flopping directions and liquid temperature, respectively. The bottom figures show schematics of the encoded states. (**C**) Flow control to obtain a sequence of the eight states (see movie S7). The first drainage bends the fin (yellow boxes), and the second drainage is to empty the cell (gray boxes), drawn according to the legend bar. The working fluid is mineral oil and q = 25 ml/min. Scale bar, 10 mm. (**D**) Example of the application of pixelated flap4s for signaling in the optical and IR domains.

roughly 1000 W for the same screen size. We expect that miniaturizing the fabrication of each flap4 cell down to 1-mm scale would open more applications. At this scale, the cells will be capable of operating in any orientation with respect to gravity, unlike the current cell size, which is influenced by gravitational effects (see section S9). This will enable uses in billboards, stadium displays, train and bus station signage, and on the facades of structures and buildings and offer significant energy reductions.

MATERIALS AND METHODS

Experimental methods

To control the fin-bending state, we connect syringe pumps (NE-1000, New Era Pump Systems) to the devices and vary the flow rate. We mount a digital single-lens reflex (DSLR) camera (EOS-904D, Canon) on top of the device to optically capture the texture switching of the flexible fins. For the side-view experiments (the bottom images of Fig. 1), we attach a glass slide to the side of the device, whereby replacing the elastomeric wall produces side see-

through devices. Figure S1A shows the schematics of the overall experimental setup.

Fabrication methods and materials

We use CAD software (SolidWorks, Dassault Systemes) to design negative molds for the devices and produce them with a 3D printer (Micro cDLM, Envision Tech) using a proprietary material from EnvisionTec called E-partial resin. After cleaning the mold by isopropyl alcohol, we put a small droplet of the silicone polymer (Elite Double 8, Zhermack) on the small fin spacing, and then the polymer droplet spontaneously wets through the spacing by capillarity. We use mineral oil as the liquid medium (light mineral oil, Spectrum) since the organic liquid wets the silicone polymer well. Only for the letter display case (Fig. 3), we use water to make the convex liquid curvature at the initial state. The liquid properties are listed in table S1.

Figure S1B shows the smallest flap4 device, which is smaller than a dime. We typically add a small amount of colored dye (less than 3 weight %) to distinguish between the fin and body colors. Depending on the device design, we used black (single and double fins and domino), red (flower), and blue (display) dyes for the different fin colors. To mix the silicone effectively, we use a centrifugal mixer (AR-100, Thinky). After filling the fin spacing with colored silicone, we pour the same polymer into the mold to fill the wall parts. We then detach the devices from the mold. The detailed fabrication steps can be shown in Fig. 1C. To measure the elastic modulus, we use the universal testing machine (DMA-850, TA Instruments). We run the tests eight times and obtain $E = 274 \pm 36$ kPa. For Poisson's ratio of the silicone polymer, v = 0.49.

Supplementary Materials

This PDF file includes:

Supplementary Materials and Methods Sections S1 to S9 Figs. S1 to S12 Tables S1 and S2 Legends for movies S1 to S7 References

Other Supplementary Material for this manuscript includes the following:

Movies S1 to S7

REFERENCES AND NOTES

- J. Teyssier, S. V. Saenko, D. van der Marel, M. C. Milinkovitch, Photonic crystals cause active colour change in chameleons. *Nat. Commun.* 6, 6368 (2015).
- J. B. Messenger, Cephalopod chromatophores: Neurobiology and natural history. *Biol. Rev.* 76, 473–528 (2001).
- J. P. Vigneron, J. M. Pasteels, D. M. Windsor, Z. Vértesy, M. Rassart, T. Seldrum, J. Dumont, O. Deparis, V. Lousse, L. P. Biró, D. Ertz, V. Welch, Switchable reflector in the Panamanian tortoise beetle *Charidotella egregia* (Chrysomelidae: Cassidinae). *Phys. Rev. E. Stat. Nonlin.* Soft Matter Phys. 76, 031907 (2007).
- 4. J. W. Weisel, C. Nagaswami, R. O. Peterson, River otter hair structure facilitates interlocking to impede penetration of water and allow trapping of air. *Can. J. Zool.* **83**, 649–655 (2005).
- 5. S. S. N. Gorb, Attachment Devices of Insect Cuticle (Kluwer, 2001).

- R. F. Shepherd, F. Ilievski, W. Choi, S. A. Morin, A. A. Stokes, A. Mazzeo, X. Chen, M. Wang, G. M. Whitesides, Multigait soft robot. *Proc. Natl. Acad. Sci. U.S.A.* 108, 20400–20403 (2011).
- J. H. Pikul, S. Li, H. Bai, R. T. Hanlon, I. Cohen, R. F. Shepherd, Stretchable surfaces with programmable 3D texture morphing for synthetic camouflaging skins. Science 358, 210–214 (2017).
- E. Siéfert, E. Reyssat, J. Bico, B. Roman, Bio-inspired pneumatic shape-morphing elastomers. Nat. Mater. 18, 24–28 (2019).
- M. A. Unger, H.-P. Chou, T. Thorsen, A. Scherer, S. R. Quake, Monolithic microfabricated valves and pumps by multilayer soft lithography. Science 288, 113–116 (2000).
- M. D. Volder, D. Reynaerts, Pneumatic and hydraulic microactuators: A review. J. Micromech. Microeng. 20, 043001 (2010).
- H.-Y. Kim, L. Mahadevan, Capillary rise between elastic sheets. J. Fluid Mech. 548, 141 (2006)
- J. Hwang, J. Ha, R. Siu, Y. S. Kim, S. Tawfick, Swelling, softening, and elastocapillary adhesion of cooked pasta. *Phys. Fluids* 34, 042105 (2022).
- J. Ha, Y. S. Kim, K. Jiang, R. Siu, S. Tawfick, Hydrodynamic elastocapillary morphing of hair bundles. *Phys. Rev. Lett.* 125, 254503 (2020).
- J. Ha, Y. S. Kim, R. Siu, S. Tawfick, Dynamic pattern selection in polymorphic elastocapillarity. Soft Matter 18, 262–271 (2022).
- A. Hadjittofis, J. R. Lister, K. Singh, D. Vella, Evaporation effects in elastocapillary aggregation. J. Fluid Mech. 792, 168–185 (2016).
- C. C. Chiao, J. K. Wickiser, J. J. Allen, B. Genter, R. T. Hanlon, Hyperspectral imaging of cuttlefish camouflage indicates good color match in the eyes of fish predators. *Proc. Natl. Acad. Sci. U.S.A.* 108, 9148–9153 (2011).
- D. J. Kemp, M. F. Herberstein, L. J. Fleishman, J. A. Endler, A. T. Bennett, A. G. Dyer, N. S. Hart, J. Marshall, M. J. Whiting, An integrative framework for the appraisal of coloration in nature. *Am. Nat.* 185, 705–724 (2015).
- P. Rothemund, A. Ainla, L. Belding, D. J. Preston, S. Kurihara, Z. Suo, G. M. Whitesides, A soft, bistable valve for autonomous control of soft actuators. Sci. Robot. 3, eaar7986 (2018).
- T. Chen, M. Pauly, P. M. Reis, A reprogrammable mechanical metamaterial with stable memory. Nature 589, 386–390 (2021).
- D. Rus, M. T. Tolley, Design, fabrication and control of soft robots. *Nature* 521, 467–475 (2015).
- C. Hu, S. Pané, B. J. Nelson, Soft micro- and nanorobotics. Annu. Rev. Control Robot. Auton. Syst. 1, 53–75 (2018).
- P. Grandgeorge, N. Krins, A. Hourlier-Fargette, C. Laberty-Robert, S. Neukirch, A. Antkowiak, Capillarity-induced folds fuel extreme shape changes in thin wicked membranes. *Science* 360, 296–299 (2018).
- J. Heikenfeld, P. Drzaic, J. S. Yeo, T. Koch, Review paper: A critical review of the present and future prospects for electronic paper. J. Soc. Inf. Disp. 19, 129–156 (2011).
- M. R. Fernández, E. Z. Casanova, I. G. Alonso, Review of display technologies focusing on power consumption. Sustainability 7, 10854–10875 (2015).
- 25. W. E. Wilson, Positive Displacement Pumps and Fluid Motors (Pitmann Pub. Co. Corp. 1950).
- L. D. Mauck, C. S. Lynch, Piezoelectric hydraulic pump development. J. Intell. Mater. Syst. Struct. 11, 758–764 (2000).

Acknowledgments

Funding: This work was supported by the AFOSR Young Investigator Program (grant no. FA9550-19-1-0010) and the NSF CMMI (grant no. 1825758). **Author contributions:**Conceptualization: J. Ha, Y.S.K., and S.T. Methodology: J. Ha, Y.S.K., J.Hw., S.C.L., R.S., and S.T. Investigation: J. Ha, Y.S.K., C.L., and S.T. Visualization: J. Ha, Y.S.K., J.Hw., and S.T. Supervision: S.T. Writing—original draft: J. Ha, Y.S.K., and S.T. Writing—review and editing: J. Ha, Y.S.K., and S.T. Competing interests: The authors declare that they have no competing interests. **Data and materials availability:** All data needed to evaluate the conclusions in the paper are present in the paper and/or the Supplementary Materials.

Submitted 14 February 2023 Accepted 30 May 2023 Published 30 June 2023 10.1126/sciadv.adh1321

Downloaded from https://www.science.org at University of Illinois - Urbana on December 22, 2023

Science Advances

Polymorphic display and texture integrated systems controlled by capillarity

Jonghyun Ha, Yun Seong Kim, Chengzhang Li, Jonghyun Hwang, Sze Chai Leung, Ryan Siu, and Sameh Tawfick

Sci. Adv. 9 (26), eadh1321. DOI: 10.1126/sciadv.adh1321

View the article online

https://www.science.org/doi/10.1126/sciadv.adh1321

Permissions

https://www.science.org/help/reprints-and-permissions

Use of this article is subject to the Terms of service